4
Experimentation

This chapter presents the design of experiments technique used for mixture design, flux preparation, and the characterization methods for flux and bead-on-plate experiments. The criteria for flux selection are then discussed. The selected electrode coating fluxes, along with a commercial electrode, were used to prepare the weld. Mechanical, metallurgical, and cathodic charging experiments are also discussed. Finally, one of the welds was selected, and details of ductile fracture experiments and simulations for both the weld and the base metal are provided.

4.1 FLUX FORMULATION AND BEAD-ON-PLATE EXPERIMENTS

4.1.1 Design of experiments

The design of experiments was done using extreme vertices design approach. The extreme vertices design is a particular case of the response surface method when the input factors have constraints. This method is well suited for mixture design experiments (McLean et al., 1966). The mixture design with $'q'$ constituents having proportions $'a_i'$ is shown in equation (4.1). The constraints of the proportion are shown in equation (4.2).

$$\sum_{i=1}^{q} a_i = 100. \tag{4.1}$$

$$0 \leq \alpha_i \leq a_i \leq \beta_i \leq 100. \tag{4.2}$$

where i =1, 2, 3, …, q and α_i and β_i are the lower and upper bounds of the constituent's proportion a_i.

The designed SMAW electrode coating flux was a multi-component system. Four major flux constituents were selected as parameters, and the rest of the constituents were kept constant. The coatings have been designed with a focus on high fluoride content (for low hydrogen), systematic substitution of CaO with BaO, and low silica and rutile powder content. The composition range of major constituents was selected from the ternary phase diagrams such as $CaF_2 - CaO - Al_2O_3$, $CaF_2 - CaO - SiO_2$ and $SiO_2 - BaO - Al_2O_3$ flux system (Allibert et al., 1995). Based on the ternary phase diagram and previous literature, composition ranges were identified to minimize the composite melting point. Table 4.1 shows the composition of the minerals used for the investigation (Mahajan et al., 2020). The XRD investigation of flux coatings are also presented in the results and discussion section. Equation (4.3) shows the mixture constraints. Two flux systems have been investigated, one system was fluoro-aluminate (AF flux) dominant and the other was fluoro-silicate (SF flux) dominant. Both the systems have same number of constituents. Lower and upper bound of the systems are shown in equation (4.4) and (4.5) respectively. The treatment combinations were generated using the Design Expert software. The design matrix for the experiments is given in Table 4.2 and 4.3. Figure 4.1, 4.2 shows the quaternary plot projections of the compositions range, and space diagram for the treatment combinations.

Table 4.1: Chemical composition of the minerals

	Mineral	Al	Ca	Fe	Mg	S	Si	Ti
1	Calcite	4.61	81.45	0.74	9.48	-	2.95	-
2	Fluorspar	4.97	92.77	0.41	-	-	1.38	-
3	Silica	2.82	0.48	0.17	-	0.29	96.16	-
4	Calcinated bauxite	83.00	4.08	0.38	-	-	1.28	-
5	Rutile	5.94	-	1.57	-	0.29	4.09	87.46

$$\sum_{i=1}^{4} x_i = 70. \tag{4.3}$$

$$\begin{gathered} 30 \leq CaF_2(x_1) \leq 38 \\ 15 \leq CaO\ (x_2) \leq 25 \\ 10 \leq Al_2O_3(x_3) \leq 18 \\ 5 \leq BaO\ (x_4) \leq 15 \end{gathered} \tag{4.4}$$

$$\begin{gathered} 5 \leq SiO_2(x_1) \leq 15 \\ 10 \leq CaO\ (x_2) \leq 20 \\ 30 \leq CaF_2(x_3) \leq 40 \\ 5 \leq BaO\ (x_4) \leq 15 \end{gathered} \tag{4.5}$$

Table 4.2: Design matrix of the experiments for fluoro-aluminate (AF) type

Flux no.	Candidate point	CaF_2	CaO	Al_2O_3	BaO
AF1	EC	34.00	21.00	10.00	5.00
AF2	V	38.00	15.00	10.00	7.00
AF3	V	30.00	17.00	18.00	5.00
AF4	EC	30.00	20.00	10.00	10.00
AF5	PC	30.00	18.00	14.00	8.00
AF6	EC	31.00	15.00	18.00	6.00
AF7	C	33.25	16.75	13.25	6.75
AF8	EC	35.00	15.00	15.00	5.00
AF9	V	38.00	17.00	10.00	5.00
AF10	EC	30.00	16.00	18.00	6.00
AF11	CE	30.00	15.00	14.00	11.00
AF12	PC	38.00	15.67	10.67	5.67
AF13	V	32.00	15.00	18.00	5.00
AF14	PC	33.60	17.80	13.60	5.00
AF15	PC	34.00	18.00	10.00	8.00
AF16	EC	38.00	16.00	10.00	6.00
AF17	EC	38.00	16.00	11.00	5.00
AF18	PC	30.67	15.67	18.00	5.67
AF19	PC	33.60	15.00	13.60	7.80
AF20	EC	30.00	21.00	14.00	5.00
AF21	EC	34.00	15.00	10.00	11.00
AF22	V	30.00	15.00	18.00	7.00
AF23	EC	31.00	16.00	18.00	5.00
AF24	EC	38.00	15.00	11.00	6.00
AF25	V	30.00	25.00	10.00	5.00
AF26	V	38.00	15.00	12.00	5.00
AF27	V	30.00	15.00	10.00	15.00

Note: -V: vertex; PC: plane centre; C: centroid; EC: edge centre;

Table 4.3: Design matrix of the experiments for fluoro-silicate (SF) type

Flux No.	Candidate point	SiO_2	CaO	CaF_2	BaO
SF1	EC	10.00	15.00	30.00	15.00
SF2	PC	8.33	20.00	33.33	8.33
SF3	EC	15.00	10.00	35.00	10.00
SF4	PC	11.67	10.00	36.67	11.67
SF5	EC	5.00	15.00	40.00	10.00
SF6	V	15.00	10.00	30.00	15.00
SF7	EC	10.00	20.00	30.00	10.00
SF8	EC	5.00	15.00	35.00	15.00
SF9	EC	10.00	10.00	35.00	15.00
SF10	EC	15.00	15.00	35.00	5.00
SF11	EC	10.00	15.00	40.00	5.00
SF12	V	5.00	20.00	30.00	15.00
SF13	EC	10.00	20.00	35.00	5.00
SF14	V	15.00	10.00	40.00	5.00
SF15	EC	10.00	10.00	40.00	10.00
SF16	C	10.00	15.00	35.00	10.00
SF17	EC	5.00	20.00	35.00	10.00
SF18	PC	15.00	13.33	33.33	8.33
SF19	PC	11.67	16.67	30.00	11.67
SF20	PC	8.33	13.33	33.33	15.00
SF21	PC	11.67	16.67	36.67	5.00
SF22	PC	8.33	13.33	40.00	8.33
SF23	V	5.00	20.00	40.00	5.00
SF24	EC	15.00	15.00	30.00	10.00
SF25	PC	5.00	16.67	36.67	11.67
SF26	V	15.00	20.00	30.00	5.00
SF27	V	5.00	10.00	40.00	15.00

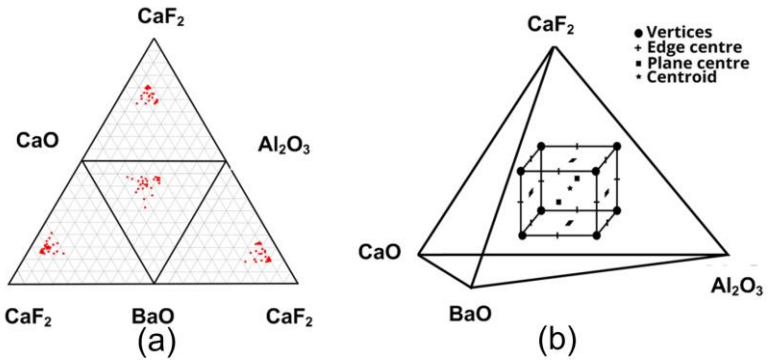


Figure 4.1: AF flux (a) Quaternary plot projections of composition range (AF flux) (b) Space diagram of treatment combinations

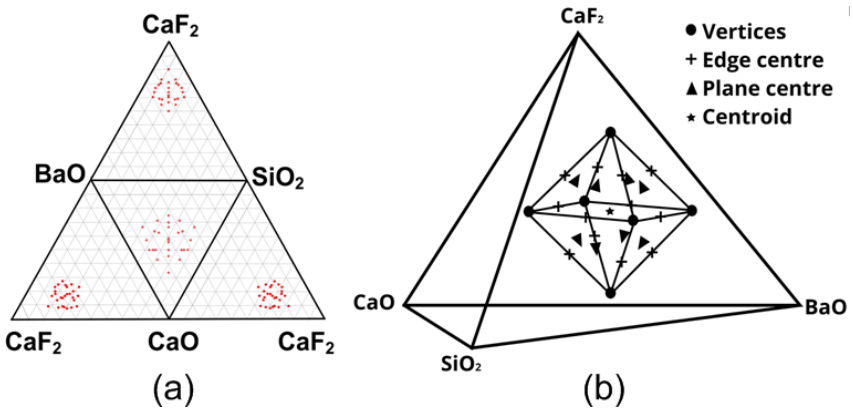


Figure 4.2: SF flux (a) Quaternary plot projections of composition range (b) Space diagram of treatment combinations

ANN modeling

The flux mixture constituents' interactions can result in synergetic and antagonistic responses, so to capture the complex behavior advance modeling techniques were adopted and compared with conventional methods. Researchers in various fields are well utilizing the concept of deep learning and machine learning. Artificial neural network (ANN) models have the ability to self-learn and self-adapt. The ANN models are very powerful in obtaining the mathematical relationship between the predictor and the response. The ANN models consist of an input layer, a hidden layer, an output layer (Li et al., 2020). The data used for ANN modeling is split into training data, validation data, and test data. The training data contains most of the data for the learning process. The overfitting of a predictive model is a major issue. An overfitted model considers noise as a signal, which affects the prediction accuracy. To avoid overfitting, the use of a validation set is widely accepted among researchers (Tian, 2012). The test data set is separate from training; it acts as unseen data for the trained model to confirm its effectiveness.

The neural net fitting ANN model was implemented using MATLAB; it is a two-layer feed-forward with sigmoid hidden neurons and linear output suitable for regression tasks. The hidden neurons have a substantial impact on the model training. Although there is no certain rule to estimate the number of hidden neurons, an empirical formula proposed by many researchers is used.

$$N_H = 0.5(N_I + N_O) + \sqrt{N_T} \tag{4.6}$$

where $N_I, N_O,\ N_T,$ and $N_H,$ are the numbers of input neurons, output neurons, training data, and hidden neurons, respectively (Li et al., 2020). In this study, 80/20, training/validation split rule is adopted to avoid overfitting. The twenty-seven flux composition is split into 22 and 5 for the training process. The three compositions were taken separately as unseen test data set to confirm the model accuracy. Using equation (4.6) number of hidden neurons is approximated as 7. The training is carried out with trial and error of hidden neurons from 5 to 10 while tracking the performance criteria of mean square error (MSE) (equation (4.7)). The prediction capability of the ANN model is verified on the new test data on the basis of mean absolute percentage error (MAPE), it is given in equation (4.8).

$$MSE = \frac{1}{n}\sum_{i=1}^{n}(Y_{actual} - Y_{predicted})^2 \tag{4.7}$$

$$MAPE = \frac{1}{p}\sum_{i=1}^{p}\left|\frac{(Y_{actual} - Y_{predicted})}{Y_{actual}} \times 100\right| \tag{4.8}$$

where n is the number of observations, p is number of predictions, Y_{actual}, and $Y_{predicted}$ are the actual and predicted results.

The ANN modeling of the experiments was done and the ANN model accuracy was compared with the conventional regression model.

4.1.2 Flux preparation

The preparation method and other tests for both the flux systems are similar so only AF flux has been discussed here and also in later sections. The fluxes were prepared by weighing and mixing the constituents as per the design matrix shown in Table 4.1. The flux constituents used in this experiment are fluorspar (CaF_2), calcite ($CaCO_3$), calcined bauxite (Al_2O_3), witherite ($BaCO_3$),

quartz (SiO_2), and rutile (TiO_2). The weight fraction of the carbonates is adjusted to achieve CaO and BaO. The flux consists of, $CaF_2 + CaO + Al_2O_3 + BaO = 70\%$, $SiO_2 = 10\%$, $TiO_2 = 10\%$, remaining 10% was ferroalloys ($Fe - Mn, Fe - Si$). Iron powder was added 20% by wt. of the total mixture weight, it was added to increase the metal deposition rate. Bentonite clay was added 2% by wt. of total mixture, to improve the coating extrudability on the electrode. The flux mixture was mechanically mixed to produce a homogenous dry mix. Finally, potassium silicate was added as a binder to produce the wet mixture. The wet mix was then air-dried for 24 hours and baked in the electric oven at 623 K (350°C) for 90 minutes. Dry flux powder was then milled and passed through the ASTM 100 sieve (150 microns). The flux powder mentioned in the later sections are dried, baked and milled powder (150 microns), which was used for the different characterizations.

4.1.3 Wettability tests

The flux powder was placed in the steel die set to produce cylindrical pellets of dimension 10 mm dia. and 10 mm height. The die set with flux powder was loaded with a force of 2 tons by using a hydraulic press. Wettability properties were measured between the flux pellet and steel substrate. Additional experimental images for pellet preparation and tests are shown in appendix Figure A2.1. The substrate plate of dimension 50 mm × 50 mm × 2 mm was used. The substrate plate was pre-oxidized by placing it in the high-temperature muffle furnace at 1073 K(900°C) for 300 seconds, this step prevents the reaction between the substrate plate and coating flux. The high-temperature muffle furnace was heated and maintained at 1573 K (1300°C) with an ambient environment. The pellets and substrate plate were then placed in the furnace for 120 seconds. The holding time of the pellet in the furnace results in degassing and setting of the molten slag on the steel substrate. The molten slag was then taken out, and it was solidified at room temperature. Images of the molten pellets were taken using a digital camera. Image analysis of the molten pellet was done to record the contact angle and spread area using ImageJ software.

Figure 4.3 (a) shows the schematic of pellet dimensions and molten pellet, and Figure 4.3 (b) shows the surface tension, contact angle, and spread area. The spreading area of the molten pellet was calculated using image analysis. The contact angle was measured geometrically and using image analysis. The contact angle was measured, and the mean of the value was taken. Figure 4.3 (c) shows the contact angle measurement.

Young's equation can be used to obtain the relationship between interfacial tensions and the contact angle. In Young's equation γ_m is the surface tension of metal (solid-vapor), γ_{ms} is the surface tension between metal-slag (solid-liquid), γ_s is the surface tension of slag (liquid-vapor), and θ is the contact angle.

$$Cos\theta = \frac{\gamma_m - \gamma_{ms}}{\gamma_s} \tag{4.9}$$

The surface tension of a multi-component slag can be estimated from the partial molar approaches (Boni et al., 1956; Nakashima et al., 1992) equation (4.10).

$$\gamma_s = x_1 \times \gamma_1 + x_2 \times \gamma_2 + x_3 \times \gamma_3 + \cdots \tag{4.10}$$

where $x_1, x_2, \ldots$ are the mole fraction, and γ_1, γ_2 are the surface tension of the pure components, also referred as the surface tension factor (Table 4.3). The temperature-dependent surface tension of BaO was derived from the literature, the surface tension of BaO was 560 mN/m at 1773 K, and the gradient was taken as -0.1 (Mills et al., 2012).

The work of adhesion (W_a) is the energy required per unit area (J/mm^2) to separate two phases viz. slag and metal. The Dupre-Young equation is used to calculate the work of adhesion equation (4.11). The floatation coefficient (Δ) was calculated using equation (4.12). The positive and higher values Δ suggest the ease of inclusion removal from the molten metal by gas bubbling. The floatation coefficient (Δ) is the difference between the work of cohesion and the work of adhesion.

$$W_a = \gamma_s \times (1 + Cos\theta) \tag{4.11}$$

$$\Delta = \gamma_s \times (1 - Cos\theta) \tag{4.12}$$

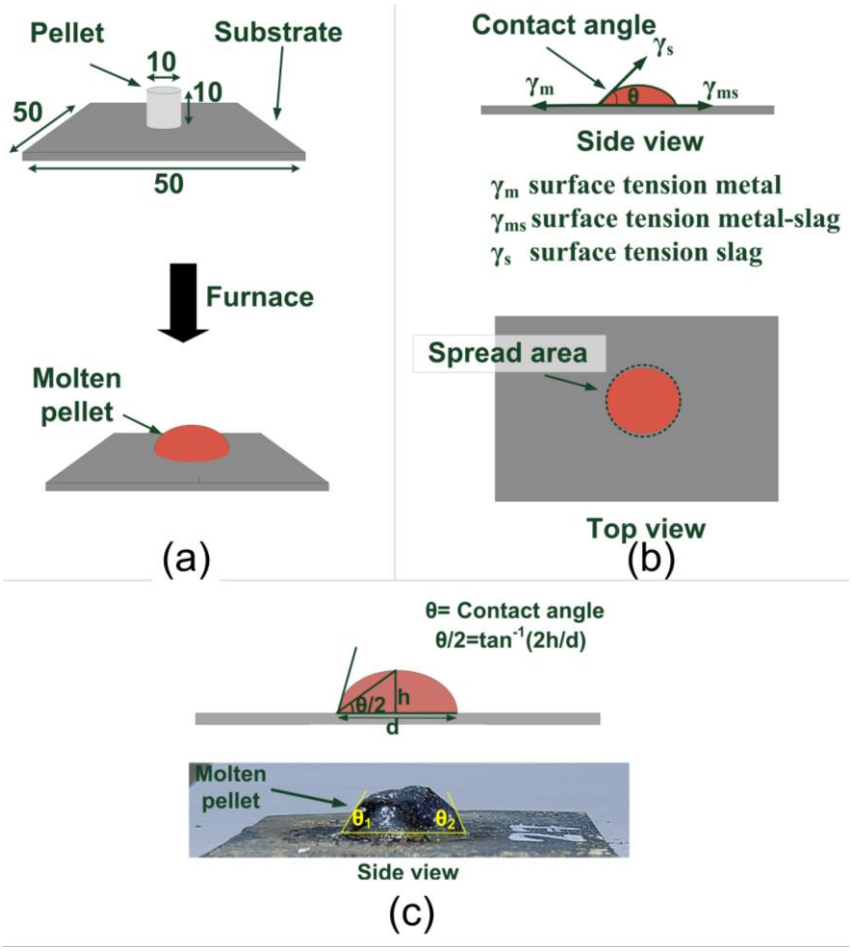


Figure 4.3: Schematic representation of (a) pellet dimensions (mm) and melting of pellets on the substrate (b) surface tension, contact angle, and spread area of the molten pellet (c) measurement of contact angle.

4.1.4 Thermophysical and physicochemical tests

Simultaneous thermal analysis (STA) of the coating fluxes was done by employing the Perkin Elmer STA6000. In STA analysis thermogravimetric analysis (TGA) is coupled with a differential scanning calorimetry (DSC). The fluxes were heated from 30℃ to 900℃ at a constant rate of 20℃/min in nitrogen environment. The weight loss and change in enthalpy obtained from the STA analysis was determined. Overall weight loss (WL) in % was calculated using below given expression:

$$\mathrm{WL}(\%) = \frac{\mathrm{W_I} - \mathrm{W_L}}{\mathrm{W_I}} \times 100\% \tag{4.13}$$

where W_I =initial weight, and W_L = least weight.

The thermal constants such as thermal conductivity, thermal diffusivity, volumetric specific heat of the coating fluxes was measured using hot disk TPS 2500s equipment. Hot disk equipment utilizes unique transient plane source (TPS) technique, which requires two pieces of specimens, and a sensor (Kapton 5465) placed in between the specimens. The process is reliable, repeatable, and needs no contact agents, fixed geometries. The specimens and equipment images are shown in appendix Figure A2.2.

Figure 4.4 (a) show the schematic for hot disk analysis and Figure 4.4 (b) show the schematic of the SMAW electrode, direction of heat flow, and thermal constants. By filling a constant volume die with wet mix, cylindrical pellets with diameters of 20 mm and height of 5 mm were made. These pellets were then baked. These pellets were used to calculate thermal constants. To ensure proper thermal contact, the pellets were polished. The density of the pellets was calculated using the weight/volume ratio. TPS analysis results in volumetric specific heat (ρC_P), which was divided by density (ρ) to produce specific heat (C_P). Equation (4.14) presents

the relationship between thermal conductivity, diffusivity, and specific heat. The flux composition has an effect on thermal constants. An increase in thermal conductivity and thermal diffusivity result in instant heat flow in the coating fluxes, which leads to an increased thermal response of the coating flux.

$$\alpha = \frac{\lambda}{\rho C_P} \tag{4.14}$$

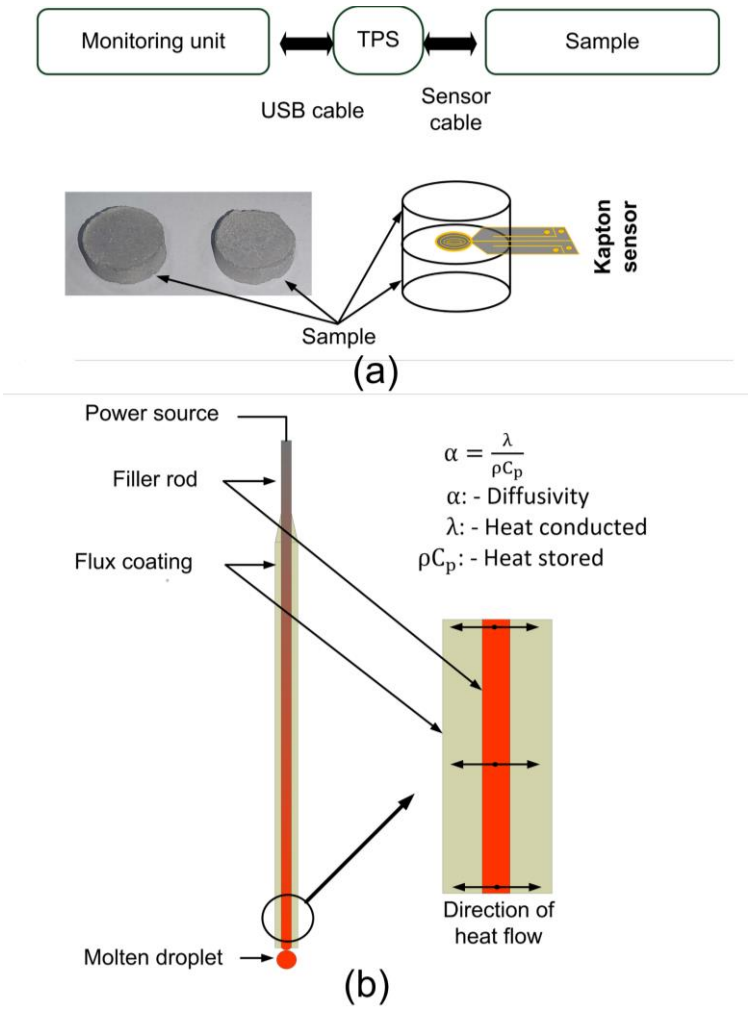


Figure 4.4: (a) schematic of hot disk analysis (b) schematic of SMAW electrode, direction of heat flow and thermal constants.

4.1.5 Theoretical estimation of flux coating behavior

During welding, plasma forms, which leads to the decomposition of oxides in slag, releases oxygen, subsequently enhancing the oxygen level inside the weld pool. The oxygen dissolution to the weld metal is primarily facilitated by welding flux. The oxygen potentials play a significant role in the system involving molten slag and metal reactions (Kou, 2003; Shao et al., 2022). The empirical relation of basicity index (BI) proposed by (Tuliani et al., 1969), is utilized for the determination of flux oxygen potential:

$$BI = \frac{CaF_2 + CaO + MgO + BaO + SrO + Na_2O + K_2O + Li_2O + 0.5(MnO + FeO)}{SiO_2 + 0.5(Al_2O_3 + TiO_2 + ZrO)} \tag{4.15}$$

The optical basicity of the multi-component flux system was calculated by the theoretical approach proposed by Duffy and Ingram (Duffy et al., 1976) equation (4.16).

$$\Lambda^{corr} = \frac{\sum x_i \times n_i \times \Lambda_i}{\sum x_i \times n_i} \tag{4.16}$$

where x_i is the mole fraction, n_i is the number of oxygens in oxide, Λ_i is the optical basicity of the pure components. The value of n_i is 2 for SiO_2, and 3 for Al_2O_3, in the case of CaF_2 is considered to have one oxygen which is equivalent to two fluorine ions. The optical basicity of CaF_2 is found to vary in literature due to the testing condition, a reasonable argument is given by Mills et al. hence a value of 1.2 is taken. The corrected optical basicity (Λ^{corr}) is calculated by using $x_{CaF2}^{corr} = x_{CaF2} - x_{Al2O3}$. The constituent having the largest Λ_i is CaF_2 whose mole fraction, i.e., x_{CaF2} is used to charge the balance the x_{Al2O3} (Mills et al., 1999). The surface tension and optical basicity data for the constituents is given in Table 4.4 (Hara et al., 1989; Liu et al., 2014; Mills et al., 2006)

Table 4.4: Surface tension and optical basicity data for the constituents

#	Constituents	Mol. wt.	γ(T)	γ at 1573K	Λ_i	n_i
1	CaF_2	78.07	$407.75 - 0.07 \times T$	297.64	1.2	1
2	CaO	56.07	$791 - 0.0935 \times T$	643.93	1	1
3	Al_2O_3	101.96	$1024 - 0.177 \times T$	745.58	0.6	3
4	BaO	153.32	$517.7 - 0.1 \times (T - 2196)$	580.00	1.15	1
5	SiO_2	60.08	$243.2 + 0.031 \times T$	297.96	0.48	2
6	TiO_2	79.86	$1384.3 - 0.6254 \times T$	400.55	0.61	2
7	Si	28.08	$850 - 0.25 \times (T - 1683)$	877.50	-	-
8	Mn	54.93	$1152 - 0.35 \times (T - 1518)$	1132.75	-	-
9	Fe	55.84	$1880 - 0.41 \times (T - 1811)$	1977.58	-	-

γ(T)=Temperature dependent surface tension (mN/m); Λ_i=Optical basicity; n_i=Number of oxygens;

The water vapor solubility of the slag substantially influences the amount of hydrogen absorbed by the molten weld metal from the arc. In general, increasing the water capacity of the slag reduces the hydrogen content of the diffusible weld metal. Water vapor solubility in slag is related to the square root of the water vapor pressure in the gas phase. It has been found that when the basicity of slag increases, the hydroxyl capacity drops, but achieves a minimum value at around one unit of basicity. As the basicity of slag rises, the hydroxyl capacity tends to rise. The dependence of hydroxyl capacity on slag composition can be explained by the change in condition of water vapor dissolved in the slag as slag basicity varies. This suggests that raising the basicity of the flux formulation can reduce the hydrogen concentration of the diffusible weld metal. The design and development of coating must compromise between operational properties and chemical properties (Allibert et al., 1995; Du Plessis et al., 2007). The water vapor solubility was calculated using the empirical relation $\mathrm{Log}C_{H_2O} = 12.04 - 32.63 \times \Lambda^{corr} + 32.71 \times \Lambda^{corr^2} - 6.62 \times \Lambda^{corr^3}$.

Shankar et al. refined the optical basicity term and provided a new optical basicity equation (4.17). Slag viscosity (η) of the developed flux is estimated at T=1673K temperature. Slag viscosity was calculated using equation (4.18-4.20).

$$\Lambda_{new} = \frac{\frac{\sum x_b \times n_b \times \Lambda_b}{\sum x_b \times n_b}}{\frac{\sum x_a \times n_a \times \Lambda_a}{\sum x_a \times n_a}} \quad (4.17)$$

Subscript b and a representing basic and acidic flux respectively

$$\mathrm{Ln}\frac{\eta}{T} = \mathrm{Ln}A + \frac{1000B}{T} \quad (4.18)$$

$$B = -180.67\Lambda_{new}{}^2 + 659.88\Lambda_{new} - 574.85 \quad (4.19)$$

$$\mathrm{Ln}A = -0.4327B - 13.053 \quad (4.20)$$

where A and B are Arrhenius equation constants

4.1.6 Structural characterization of flux and slag

For structural analysis of fluxes, six compositions from the extreme vertices' points were selected viz, AF2, AF3, AF9, AF13, AF22, and AF25. This selection has highest and lowest basicity

of flux. The phases present in the fluxes were analyzed using Bruker D8 advance powder X-ray diffraction (XRD). The analysis was carried out using 2θ diffraction mode in the range of 20° to 80°. The scan speed was at 2°/min. The structural behavior of the flux constituents was confirmed using Fourier transform infrared spectroscopy (FTIR) (Bruker vertex 70v, PMA50). The analysis was performed at a resolution of $2\ cm^{-1}$. The pellets were prepared with potassium bromide (KBr) as a reference.

The rapid quenching of the slag stores information about the melt structure. The coating flux was placed on the pre-oxidized substrate plate and then put in the high-temperature muffle furnace for melting. The molten slag was rapidly quenched in cold water to produce the amorphous slag (Wang et al., 2022). The quenched slag was collected mostly from the top of the melt to prevent any possible contamination. Further processing of the slag involves drying and milling to pass through ASTM 100 sieve. For the structural analysis of the quenched slag, six selected composition fluxes were renamed as QAF2, QAF3, QAF9, QAF13, QAF22, and QAF25 for clear identification of the result from flux and its slag. The quenched slag powder was employed for the structural analysis of the melts using advanced characterization techniques such as XRD, FTIR, and UV-vis (Agilent Cary 4000).

4.1.7 Bead-on-plate experiments

The bead-on-plate (BOP) experiments were performed using an inverter-based SMAW welding machine (Rilon, TIG 400A). The welding setup and coated electrodes have been shown in Figure 4.5 (a). The trial experiments were performed, and 100 A constant current was selected for BOP experiments. Before welding, the base plates were cleaned with a surface grinder. The weld beads were then laid on a steel plate with a size of $100 \times 30 \times 6$ mm. A direct current electrode positive polarity was used; this polarity promotes high metal deposition. Five layers of weld bead were deposited to generate an undiluted weld zone. The temperature between passes was maintained between 150℃ and 200℃. Figure 4.5 (b) shows the schematic of slag metal reactions and Figure 4.5 (c) shows the weld bead using developed electrode. The test coupons were then extracted from the BOP for microhardness, metallographic analysis, and weld bead chemistry (Figure 4.5 (d)). The observation table was prepared to qualitatively judge the electrode performance during welding. The observation table had columns for slag detachability, bead appearance (uniformity of ripples), restrike requirements, and arc stability. The observation table helps for screening the electrode coatings.

4.1.8 Microhardness, and element transfer tests

Vickers microhardness test was used to determine the effect of flux composition on microhardness (ASTM E92-17). Figure 4.6 illustrates the microhardness measurement of specimens A22. The BOP specimens were loaded with 0.5 Kgf and held for 10 seconds. Five indents were made on each specimen in the undiluted zone, and the results were averaged. The weld has been intended for thick pipeline steel, in these welds large number of multi-pass is required, so negligible dilution from base metal is expected. The undiluted weld zone for chemical analysis was prepared according to the standards (AWS A5.5, 2006). The initial weld layer deposited gives dilution with base metal, which is reduced by the successively deposited welds. The uppermost layer contains a negligible amount of base metal chemical composition. Also, electrode positive polarity melts the electrode more rapidly than the base metal, which reduces the dilution. Considering the maximum dilution of 30% in SMAW weld, it will be reduced to 0.8% in the third layer, followed by 0.006% and nearly 0% for the fifth layer, so five layers were deposited. Also, the intention was to examine the role of flux coating in loss or gain of elements in the undiluted weld zone. So, the microhardness study was done only for the undiluted weld zone to see the influence of flux composition. The response 'MH' stands for the specimens' microhardness (HV).

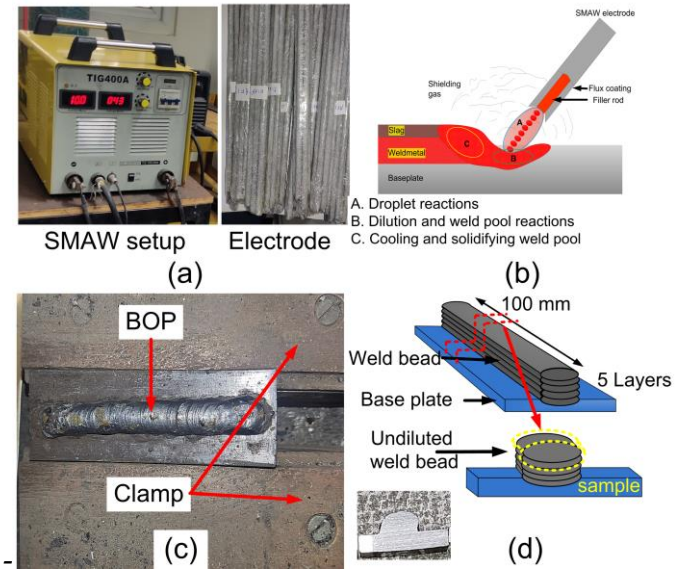


Figure 4.5: (a) welding setup and developed electrode (b) Schematic of slag metal reactions (Mitra et al., 1991) (c) weld bead using developed electrode (d) schematic for specimens extraction

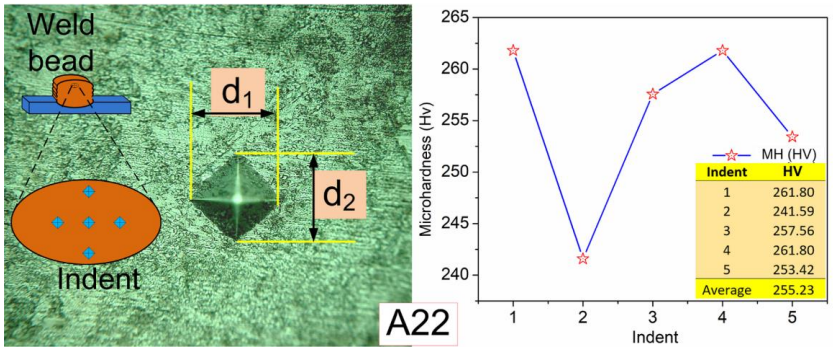


Figure 4.6: Microhardness measurement of the specimens A22

The weld chemistry is governed by the alloying element present in the electrode rod, but its transmission is governed by the slag metal interaction. As a result, the calculation of alloying element transfer from electrode rod to weld pool is connected with the fluctuation in flux composition. The undiluted weld zone chemistry is exclusively determined by the composition of the electrode rod and flux. The bare electrode rod for coating has designation of ER80S Ni1 classification, and is compatible with API X70 steel (AWS A5.28). The main alloying elements of bare electrode rod are: Ni=1.01%, Mo=0.257%, and Mn=1.1%. X-ray fluorescence was used to examine the weld chemistry of the specimens. δE represents the difference in element weight %, where E stands for element wt%:

$$\delta E = E_{BOP} - E_{electrode} \quad (4.21)$$

where E_{BOP} is the element weight percentage of undiluted weld bead and $E_{electrode}$ is the element weight percentage of electrode rod. The δE will show comparable increases and decreases from the electrode rod.

4.2 SELECTION OF FLUX

After the testing and characterization of the flux and BOP experiments. Better performing electrode coatings were screened. The primary function of the coating flux is slag detachability, weld bead appearance, low restrike requirements. First screening was done for fulfilling the primary function. Secondary functions were low WL%, weld chemistry, low wettability, and thermal diffusivity. Using these criteria one flux from each system was selected for the welding.

The coatings have been designed with a focus on high fluoride content, systematic substitution of Ca0 with Ba0, and low rutile and silica powder content. Table 4.5, 4.6 shows the visual observation table prepared during the welds performed using developed electrode coatings. The qualitative analysis was done on the basis of arc stability i.e., continuous arc during weld, slag detachability is the ease of slag removal, weld bead appearance was judged for uniformity of ripple, and high restrike means poor restarting of arc during weld and low restrike requirement is desirable. If the electrode coating is poor, the electrode rod melts quickly, leaving a hard coating at the tip. This necessitates restriking the electrode to restart the diminished arc. In contrast, a good coating melts evenly along with the electrode rod, making it easier to restart the arc if it diminishes during welding.

Table 4.5: Visual observation table prepared during welds using AF flux

Bead No.	Arc stability	Slag detachability	Appearance	Restrike
A1	Good	Poor	Poor	Low
A2	Avg.	Avg.	Avg.	High
A3	Avg.	Avg.	Avg.	High
A4	Good	Poor	Poor	Low
A5	Good	Good	Good	Low
A6	Good	Good	Good	Low
A7	Good	Avg.	Avg.	High
A8	Avg.	Poor	Avg.	High
A9	Avg.	Avg.	Avg.	High
A10	Poor	Avg.	Poor	High
A11	Good	Avg.	Avg.	Low
A12	Good	Avg.	Avg.	Low
A13	Poor	Avg.	Avg.	High
A14	Avg.	Avg.	Good	Low
A15	Avg.	Avg.	Avg.	Low
A16	Good	Good	Good	Low
A17	Good	Avg.	Poor	High
A18	Avg.	Avg.	Avg.	Low
A19	Good	Good	Good	Low
A20	Avg.	Poor	Poor	Low
A21	Good	Good	Avg.	Low
A22	Good	Avg.	Good	Low
A23	Poor	Avg.	Avg.	High
A24	Avg.	Good	Good	High
A25	Avg.	Poor	Poor	High
A26	Good	Good	Good	Low
A27	Avg.	Avg.	Avg.	High
VA28	Avg.	Poor	Avg.	Low
VA29	Avg.	Avg.	Avg.	Low
VA30	Good	Good	Good	Low

Table 4.6: Visual observation table prepared during welds using SF flux

Bead No.	Arc stability	Slag detachability	Appearance	Restrike
S1	Good	Good	Good	Low
S2	Good	Good	Good	Low

S3	poor	Avg.	Avg.	High
S4	poor	Avg.	Avg.	Low
S5	Good	Good	Good	Low
S6	Avg.	Good	Good	High
S7	Avg.	poor	poor	High
S8	Good	Avg.	Good	Low
S9	Good	Avg.	Avg.	Low
S10	Avg.	Avg.	poor	High
S11	poor	poor	poor	High
S12	Avg.	Avg.	Good	Low
S13	Avg.	Good	Avg.	High
S14	poor	poor	poor	High
S15	Good	Good	Avg.	Low
S16	Avg.	Avg.	Avg.	High
S17	poor	poor	poor	High
S18	Avg.	Avg.	Avg.	High
S19	Good	Good	Good	Low
S20	Good	Good	Good	Low
S21	poor	poor	poor	High
S22	Good	Good	Good	Low
S23	Good	Good	Good	Low
S24	Avg.	Avg.	poor	Low
S25	Good	Good	Good	Low
S26	Good	Good	Good	Low
S27	Good	Good	Good	Low
VS28	Avg.	Good	Avg.	Low
VS29	Good	Avg.	Avg.	Low
VS30	Avg.	Avg.	Avg.	Low

The SMAW coating consists of flux SiO_2, CaO, CaF_2, BaO, TiO_2, Al_2O_3 alloying element FeMn, FeSi, FeNb, Ni, potassium silicate binder, and 15% Iron powder was added for deposition efficiency. Bentonite clay was added 2% by wt. of total mixture, to improve the coating extrudability on the electrode. Table 4.7 shows the finally selected SMAW coating fluxes, this composition has been tuned as per the past experience. The selected coating was extruded on the ER80S-Ni1 rod with 3.2 mm dia. and 350 mm length. The extrusion process is shown in appendix Figure A2.3 The ratio of coated to bare rod diameter, i.e., coating factor, was ~1.65. For comparison, the welding was also performed using commercial E8018-G electrode. The flux composition of E8018-G was examined using XRF analysis (Table 4.8). It can be seen that the commercial electrode coating is mainly calcite and quartz mineral.

Table 4.7: Final flux composition

#	CaF_2	CaO	Al_2O_3	BaO	SiO_2	TiO_2	FeSi	FeMn	FeNb	Ni
AF	40.2	15.9	12.7	5.3	8.0	8.0	1	6	2	1
SF	31.7	15.9	8.0	15.9	10.6	8.0	1	5	2	2

Table 4.8: XRF result of E8018-G coating

	SiO_2	CaO	TiO_2	Al_2O_3	Fe_2O_3	MnO	Na_2O	K_2O	MgO	NiO
E8018G	19.5	50.6	1.2	0.6	7.8	2.4	2.7	3.5	0.7	0.4

4.3 MATERIALS AND WELDMENT PREPARATION

The base plate material for welding was a 22 mm thick plate of API X70 steel. The ER80S-Ni1 rod was coated with the formulated fluxes, i.e., AF and SF flux, the welds produced using these electrodes are AF_W, and SF_W, respectively. Shielded metal arc welding was used to produce three weld joints; two joints by using laboratory developed electrode and one by a commercial E8018-G electrode.

The groove of 60° V butt weld was prepared using a shaper machine. The root face was 2 mm. The weld groove was cleaned mechanically and chemically to remove oil and dirt. Tack welding was done to keep a root gap of 2 mm. Tack plates were welded to prevent distortion of the plate and to keep the root gap steady during welding (Alipooramirabad et al., 2017). The base plates were pre-heated to 150℃, and the root pass was laid on all three joints using the E6010 cellulosic electrode, A constant current of 100 Amp (I) was used. The root passes are generally undermatched, also, low heat input is used to prevent root defects. After the root pass, the weld AF_W and SF_W were produced using laboratory developed electrodes, and the weld CE_W was produced using a commercial E8018-G electrode. A constant current of 124 Amp (I) was used for laying the weld, the welding speed was nearly 2.4 mm/s (S). During welding, the arc voltage was recorded using a multimeter, average of 24 V was calculated. The heat input can be calculated from the equation $\mathrm{HI} = f \times \mathrm{VI/S}$, where f=0.8 is process efficiency for SMAW. The heat input was estimated to be nearly 0.992 KJ/mm for all passes and 0.8 KJ/mm for the root pass. The interpass temperature was maintained nearly ~250℃. The standard procedure for welding requires the baking of basic electrodes prior to weld, although in this work the electrodes were not baked prior to welding. Welding was performed with the electrodes in as-is condition, this practice was opted to compare the electrodes with environmental exposure. Welds were cooled down in the ambient air, and the testing specimens were extracted from the as weldment. The schematic of welding, welded plate, and the sequence of weld deposition is shown in Figure 4.7 (a-c). Table 4.9 shows the parameters used during the welding.

Table 4.9: Parameters of welding procedure

Parameter	Welding	Unit
Welding position	1G Flat	–
Groove design	60° V groove butt joint	–
Polarity	DCEP (CC)	–
Plate thickness	22	mm
Current (I)	124	Amp
Arc voltage (v)	24	V
Electrode diameter	3.2	mm
Welding speed	2.4	mm/s
Heat input (all)	0.992	KJ/mm
Heat input (root)	0.8	KJ/mm
Preheating temperature	~150	℃
Interpass temperature	~250	℃

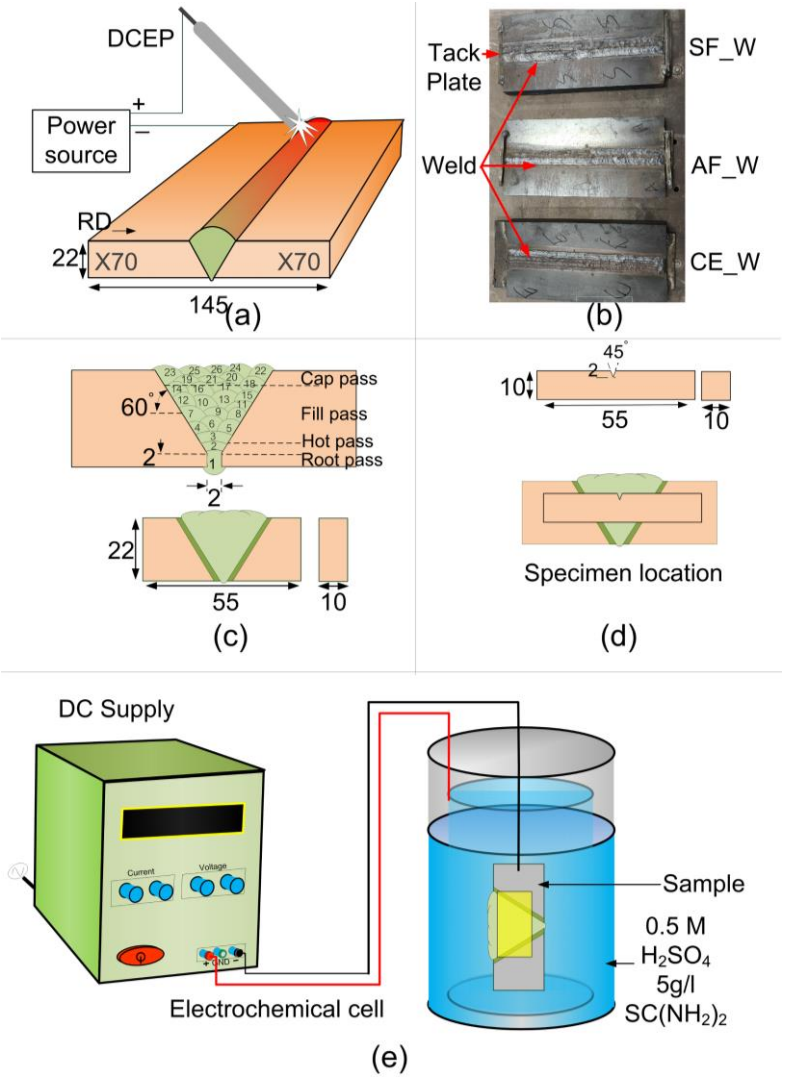


Figure 4.7: (a) schematic of SMAW and plate dimensions, (b) Welded plates, (c) Multi-pass weld and specimen dimension, (d) Impact specimen dimension, (e) Cathodic charging

4.3.1 Microstructural and mechanical tests

The specimens were extracted for microstructure, microhardness, impact, and tensile tests. The dimension of the extracted specimen is shown in Figure 4.7 (c, d) and Figure 4.8 (a). The specimen for microstructure study was polished from 120 to 2000 grit SiC emery paper, followed by alumina polishing. The etching was performed using 5% Nital solution (30 s). Leica microscope (DMC4500) was employed to investigate the weld and base metal microstructure. The SEM-Carl Zeiss, EVO-18 instrument was used for scanning electron microscopy (SEM) of the specimen, and energy dispersive spectroscopy (EDS) was done with Oxford instruments. specimens were 2% Nital etched for the SEM investigation. The Vickers microhardness test is essential for evaluating welds, it reveals differences in hardness between the weld, heat-affected zone, and base metal (ASTM E92). The hardness variation in the weldment was investigated from the cap to the root, as well as from the weld center to the HAZ and the base metal. The hydrogen charged specimens were also investigated using the hardness test. The hardness test load was 0.5 Kgf which was held for 10 s. The hardness measurement on the weld was done from cap to root pass at 1 mm of spacing. Similarly, hardness indent from weld centerline to HAZ were taken, in the HAZ region 0.5 mm gap was given between the indent. The Charpy V-notch test of the weld and X70 base metal was done to assesses the ability to absorb impact energy. The dimensions of the impact specimen are shown in Figure 4.7 (d) (ASTM E23). Three specimens were tested and the average results was determined. Uniaxial tensile test was performed on the flat subsize tensile specimen

(ASTM E8/E8M). The tests were performed at 1mm/min displacement rate. The gauge length of the tensile specimens 25 mm. DIC was used to measure the strain. The fracture specimens were then cut for the area reduction measurement and fractography analysis. Experimental images of the tested specimens are shown in appendix Figure A2.4.

Additionally, thermodynamic model MUCG83 was used to plot TTT and CCT curves for weld and base metal. Phase fraction microhardness vs. cooling rate of the welds was estimated using thermodynamic model. The equilibrium phase diagram for the welds was generated using OpenCalphad technique by utilizing materials square thermodynamic database.

4.3.2 Cathodic charging of specimens

The cathodic charging technique was utilized to ingress the hydrogen in the specimen. Specimens were polished up to 2000 grit paper, followed by cloth polishing. Various researchers have adopted cathodic charging techniques due to their safety, ease, and good imitation of sour conditions with standard H_2S promoted charging. The specimen was immersed in a 0.5 M sulfuric acid+5g/l thiourea solution. A DC power source was used to supply 50 mA/cm^2 current density for 10 h (Latifi et al., 2017; Zhang et al., 2024). The electrochemical cell contains specimen as cathode and SS304 net as anode. Only a small surface area of 2.5×1.5 cm^2 was exposed, whereas the rest of the specimen was covered with enamel to prevent exposure. The schematic of cathodic charging is shown in Figure 4.7 (e). The hydrogen charged specimens were then cleaned with water and then ethanol. Microhardness test of the specimens with and without charging was done. Two tensile test specimens from each weld and base were hydrogen charged. In tensile specimen charging two faces of gauge length (25 mm) were exposed to solution.

4.4DUCTILE FRACTURE AND FINITE ELEMENT ANALYSIS

4.4.1 Experiments

As per the results obtained from the weld characterization, AF_W weld was selcted for the ductile fracture investigation. The dimensions of the base metal (BM) and weld metal (WM) tensile specimens are shown in Figure 4.8 (a). The gauge length of 25 mm was considered for strain calculation. Flat tensile and flat notch tensile bars (R2 mm) were tested at 1 mm/min displacement rate. Images were acquired at 1 frame per second during the test considering the quasi-static analysis. Digital image correlation (DIC) was used to determine the strain.

The SENB specimen dimensions conform to the standards (ASTM E1820). The SENB specimen from the weld has been extracted in the location of the weld centerline. The SENB dimnesions (mm) are $W = 16, B = 8, S = 64$. The Figure 4.8 (b-d) shows the schematic of the SENB specimen, EDM cut crack, SENB specimens and experimental test setup. The BM SENB has a 25% side groove, and WM SENB has a 10% side groove. Two levels of constraints were tested i.e., high $a_o/W = 0.50$, and low constraints $a_o/W = 0.25$. Two tests were performed for each specimen. The pre-crack was introduced by electric-discharge machining (EDM). Precise a_o/W can be prepapred using the EDM, although notch acuity is comparitively higher than the fatigue pre-cracking method. Present work has utilized EDM-cut SENB specimens to calibrate GTN model parameters, these parameters are then validated on different geometry.

DIC was used to determine the crack mouth opening displacement (CMOD). For the analysis, speckle patterns were created on the specimens. DIC is a powerful optical technique that can track the speckle pattern. Since the tests are quasistatic in nature, images were recorded at 1 frame per second. ZEISS INSPECT Correlate software was used for DIC. The steps followed for the DIC were; 1. Importing images, 2. Defining scale, 3. Surface component genration (facet size ≈ 36 Pixels, point distance ≈ 30 Pixels), 4. Consruct extensometer, 5. Distance calculation and 6. Export data. The tracking of crack propagation using digital image correlation was dificult. Crack growth $\Delta a_o = (a_i - a_o)$ was measured using image analysis. Figure 4.8 (e) shows CMOD measurement using DIC.

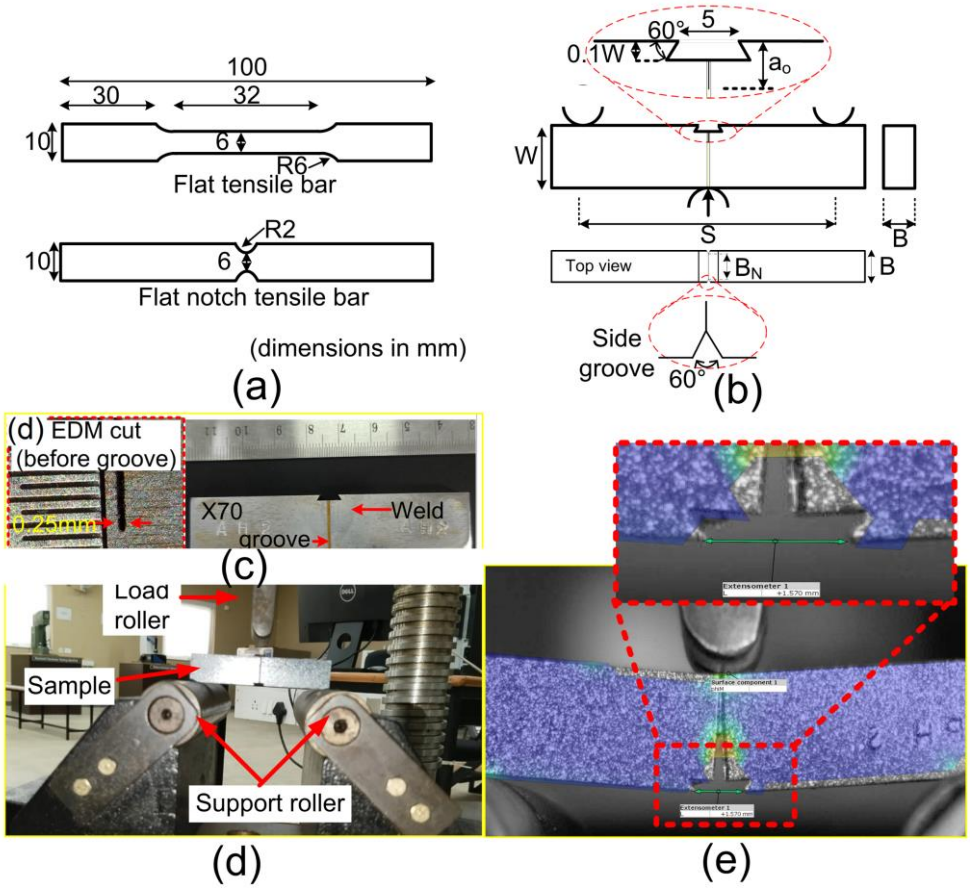


Figure 4.8: (a) Dimensions of flat tensile specimens, (b) Schematic of SENB specimen (c) EDM cut crack and SENB specimens, (d)Experimental test setup for SENB (e) CMOD measurement using DIC

4.4.2 J integral

The procedure for the calculation of J − integral of SENB specimen is given by the ASTM E1820. CMOD-based incremental formulas (Equation (4.22-4.25)) were used for the calculation of J − integral values.

$$K_{(i)} = \left[\frac{P_i S}{(BB_N)^{\frac{1}{2}}(\mathrm{W})^{\frac{3}{2}}}\right] f\left(\frac{\mathrm{a}_i}{\mathrm{W}}\right) \tag{4.22}$$

$$f\left(\frac{\mathrm{a}_i}{\mathrm{W}}\right) = \frac{3\left(\frac{\mathrm{a}_i}{\mathrm{W}}\right)^{\frac{1}{2}}\left[1.99 - \left(\frac{\mathrm{a}_i}{\mathrm{W}}\right)\left(1 - \left(\frac{\mathrm{a}_i}{\mathrm{W}}\right)\right)\left(2.15 - 3.93\left(\frac{\mathrm{a}_i}{\mathrm{W}}\right) + 2.7\left(\frac{\mathrm{a}_i}{\mathrm{W}}\right)^2\right)\right]}{2\left(1 + 2\frac{\mathrm{a}_i}{\mathrm{W}}\right)\left(1 - \frac{\mathrm{a}_i}{\mathrm{W}}\right)^{\frac{3}{2}}} \tag{4.23}$$

$$\mathrm{J}_{(i)} = \frac{\left(K_{(i)}\right)^2(1-\nu^2)}{E} + \mathrm{J}_{pl(i)} \tag{4.24}$$

$$\mathrm{J}_{pl(i)} = \left[\mathrm{J}_{pl(i-1)} + \left(\frac{\eta_{pl(i-1)}}{b_{(i-1)}}\right)\left(\frac{A_{pl(i)} - A_{pl(i-1)}}{B_N}\right)\right] \times \left[1 - \gamma_{pl(i-1)}\left(\frac{a_{(i)} - a_{(i-1)}}{b_{(i-1)}}\right)\right] \tag{4.25}$$

Where K is stress intensity factor, P is load, J_{pl} is plastic part of J − integral, J is J − integral,
For the sake of completeness remaining formulas are given in the appendix.
The fracture instability before stable tearing was observed in weld. The fracture instability toughness values (J_{Qc}) for weld were calculated according to the ASTM E1820.
The load-CMOD area was used for the calculation of area (plastic)

$$A_{pl(i)} = A_{pl(i-1)} + \frac{[P_{(i)} + P_{(i-1)}][\mathrm{v}_{pl(i)} - \mathrm{v}_{pl(i-1)}]}{2} \tag{4.26}$$

$A_{pl(i)}$ is plastic area part of load-CMOD curve, $P_{(i)}$ is load, $\mathrm{v}_{pl(i)}$ is plastic part of CMOD which can be calculated using formula given below:

$$v_{pl(i)} = v_{(i)} - \left(P_{(i)}.C_{(i)}\right) \tag{4.27}$$

$(P_{(i)}.C_{(i)})$ is elastic CMOD and $C_{(i)}$ is compliance which can be calculated as follows:

$$C_{(i)} = \frac{6S}{EWB_e}\left(\frac{a_i}{W}\right) \times \left[0.76 - 2.28\left(\frac{a_i}{W}\right) + 3.87\left(\frac{a_i}{W}\right)^2 - 2.04\left(\frac{a_i}{W}\right)^3 + \frac{0.66}{\left(1-\frac{a_i}{W}\right)^2}\right] \tag{4.28}$$

$$B_e = B - \frac{(B-B_N)^2}{B} \tag{4.29}$$

B_e is effective thickness

using above formulae $A_{pl(i)}$ was calculated for estimation of $J_{pl(i)}$.

$$\eta_{pl} = 3.667 - 2.199\left(\frac{a_{i-1}}{W}\right) + 0.437\left(\frac{a_{i-1}}{W}\right)^2 \tag{4.30}$$

and

$$\gamma_{pl} = 0.131 - 2.131\left(\frac{a_{i-1}}{W}\right) + 1.465\left(\frac{a_{i-1}}{W}\right)^2 \tag{4.31}$$

Calculation of CTOD (δ)

$$\delta_i = \frac{J_i}{m_i \sigma_Y} \tag{4.32}$$

$$m = A_0 - A_1\left(\frac{\sigma_{YS}}{\sigma_{UTS}}\right) + A_2\left(\frac{\sigma_{YS}}{\sigma_{UTS}}\right)^2 - A_3\left(\frac{\sigma_{YS}}{\sigma_{UTS}}\right)^3 \tag{4.33}$$

$$A_0 = 3.18 - 0.22\left(\frac{a_i}{W}\right) \tag{4.34}$$

$$A_1 = 4.32 - 2.23\left(\frac{a_i}{W}\right) \tag{4.35}$$

$$A_2 = 4.44 - 2.29\left(\frac{a_i}{W}\right) \tag{4.36}$$

$$A_3 = 2.05 - 1.06\left(\frac{a_i}{W}\right) \tag{4.37}$$

The CTOD calculation was done for estimating the corrected crack growth. The CTOD was calculated till $a_i = a_o$.

4.4.3 Inverse approach of GTN parameters identification

The present study utilizes the inverse approach due to its ease and accuracy (Fratini et al., 1996). For steels, the parameters $q_1 = 1.5, q_2 = 1, q_3 = 2.25$, $\varepsilon_N = 0.3$ and $S_N = 0.1$ can be taken constant (Chen et al., 2021; Gholipour et al., 2019). The VVF of nucleation (f_N) was estimated from the Franklin's formula, researchers (Qiang et al., 2019; Zhang et al., 2000) have also used similar approach to find VVF of nucleation (f_N). The formula is given by equation (4.38) (Franklin, 1969).

$$f_v = 0.054 \times \left(\%S - \frac{0.001}{\%Mn}\right) \tag{4.38}$$

where Mn% and S% are the wt% of Manganese and Sulfur. The Franklin's formula calculates the VVF of MnS inclusion. MnS and oxide inclusions present in the pipeline steels play a major role in the ductile fracture process. The VVF of nucleation was calculated $f_v \approx f_N = 0.001$ for BM and 0.0018 for WM. The remaining three parameters f_o, f_c and f_f were calibrated using design of experiments.

The Box–Behnken design was used to generate different parameter combinations. The design matrix given in Table 4.10 was generated using Design Expert software. The range was determined from the previous literature and trial simulations. For the BM, the ranges for the different parameters were considered as f_o =0.0005−0.002, $f_c = 0.01 - 0.20$, and $f_f = 0.25 - 0.5$. For the WM, f_o =0.002−0.007, $f_c = 0.01 - 0.08$, and $f_f = 0.2 - 0.40$ were taken as parametric spaces. It should be noted that the range is very sensitive to material response, so a considerable trial-error may be required to obtain a suitable parameter range. The objective functions were to curve fit the experimental SENB ($a_o/W = 0.50$) load-CMOD curve and crack growth. The first objective function (Obj_1) was to fit the simulated load value at 8 mm CMOD. The other two

objectives' functions (Obj_2, and Obj_3) were to match the crack growth at 3 mm and 7 mm CMOD. The Obj_1, Obj_2, and Obj_3 were defined using the below given Equation (4.39) The target was to achieve zero value for all the objectives functions so that the simulated load-CMOD and crack growth is best fitted with experimental data.

$$\text{Obj_(1,2, and 3)} = (\text{Experiment response} - \text{Simulation response})/\text{Average} \quad (4.39)$$

After the experimentation, a quadratic polynomial regression equation can be developed as,

$$Y = \beta_o + \sum_{i=1}^{k} \beta_i . x_i + \sum \sum_{i<j} \beta_{ij} . x_i . x_j + \sum_{i=1}^{k} \beta_{ii} . {x_i}^2, \quad (4.40)$$

where Y is output, i.e., objectives functions (Obj_1, Obj_2, and Obj_3), β is coefficients of the regression equation, x_i represents individual effect, $x_i . x_j$ represents interaction effect, and ${x_i}^2$ quadratic effect of inputs (f_o, f_c and f_f). Using these mathematical models, input parameters can be tuned for the required material response.

Table 4.10: Design matrix for X70 GTN parameter calibration

#	$1 - f_o$	f_c	f_f	Obj_1	Obj_2	Obj_3
1	0.99875	0.105	0.375	1.11	-3.16	0.52
2	0.99800	0.010	0.375	4.10	23.92	7.79
3	0.99800	0.105	0.250	1.90	11.88	3.76
4	0.99950	0.010	0.375	1.71	2.86	2.14
5	0.99950	0.200	0.375	-2.39	-13.69	-4.32
6	0.99800	0.105	0.500	1.40	-3.16	0.52
7	0.99875	0.105	0.375	1.11	-3.16	0.52
8	0.99875	0.010	0.500	1.99	5.87	2.14
9	0.99875	0.105	0.375	1.11	-3.16	0.52
10	0.99875	0.105	0.375	1.11	-3.16	0.52
11	0.99875	0.010	0.250	4.34	32.95	9.41
12	0.99875	0.105	0.375	1.11	-3.16	0.52
13	0.99875	0.200	0.500	0.08	-13.69	-1.09
14	0.99950	0.105	0.250	-1.27	-6.17	-1.09
15	0.99875	0.200	0.250	0.47	2.86	0.52
16	0.99950	0.105	0.500	-2.34	-13.69	-7.55
17	0.99800	0.200	0.375	1.48	2.86	2.14

4.4.4 Simulation details

(a) Uniaxial tensile test

The Abaqus/Explicit solver was used for finite element analysis. The flat bar tensile test was modeled using a 3-dimensional quarter-symmetric domain. The displacement boundary condition (BC) was applied. Quasistatic analysis was performed by suitably selecting the step time, so that the kinetic energy was negligible as compared to internal energy of the model. The model was meshed using 8 noded linear brick element with reduced integration (C3D8R). Mesh sensitivity study was conducted with different element sizes. The element size of 0.1 mm was chosen for the simulations. Figure 4.9 (a) shows the meshing of the tensile simulation model.

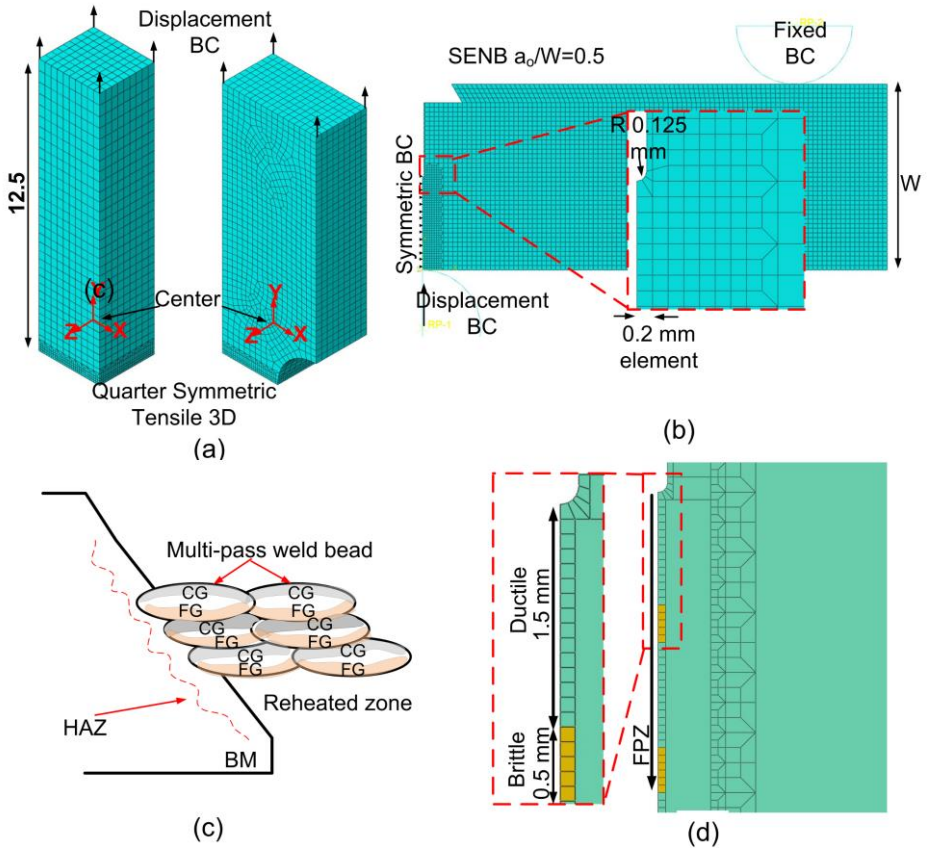


Figure 4.9: (a) Quarter symmetric 3-D simulation model of tensile bar, (b) SENB a_0/W=0.50 2-D simulation meshing (c) Schematic of the effect of reheated zone on multi-pass weld (d) Modified fracture process zone

(b) SENB test

A half-symmetric 2-dimensional model (meshed with 4 noded plane strain element with reduced integral, CPE4R) was used for modeling the SENB specimen. The support and load rollers were modeled as discrete rigid part. Hard contact surface interaction and the friction coefficient of 0.01 was selected. Figure 4.9 (b) shows the meshing for the SENB ($a_o/W = 0.50$) simulation model. Similarly, the simulation of the $a_o/W = 0.25$ SENB was set up. The crack tip radius of 0.125 mm was modeled; this dimension reflects the EDM cut on the SENB specimens. Due to the crack propagation in SENB model mesh size selection for GTN model becomes more sensitive. The load-carrying capacity of the element diminishes as the VVF reaches the value equal to f_f, also known as nodal force release. The elements adjacent to the half-plane symmetry undergo nodal force release in the fracture process zone (FPZ). The element size in the FPZ resembles the critical length parameter (l_c) which is defined as mean void spacing between the inclusions. For BM SENB 0.2 mm (l_c) mesh size was found suitable. Finally, the load roller was given a displacement boundary condition, the support roller was fixed, and FPZ was given symmetric boundary conditions.

The experimental weld SENB test has shown pop-in in WM, which is common in weld. The pop-in is a sudden drop in load-CMOD curve due to brittle fracture. The multi-pass weld by shielded metal arc welding results in fine grain and coarse grain within the weld bead. This inhomogeneity with increasing displacement results in pop-in. A modified FPZ was developed to capture the pop-in effect. The weld bead was nearly 2 mm, which contains coarse grain (CG) and fine grain (FG) (Figure 4.9 (c)). A simple inhomogeneity of 0.5 mm was added within the 2 mm weld bead. The brittle zone was assumed to have zero hardening after σ_{UTS}. The yellow section was assigned with zero hardening material property. Figure 4.9 (d) shows the modified fracture process zone (Mod_FPZ). Same Mod_FPZ was used for both SENB $a_o/W = 0.50$, and SENB $a_o/W = 0.25$. Further investigation has compared the Mod_FPZ with regular FPZ. The mesh size of 0.1 mm was used for the simulation of WM SENB.

The experimental SENB test using fatigue pre-cracking is a standard procedure for generating sharp crack tip, but this method is time consuming and does not accurately capture initial crack (a_o/W). Some researchers have used EDM cut SENB for accurate initial crack but this leads to reduced notch acuity resulting in high initial fracture toughness. Present works has targeted to model EDM cut SENB using GTN damage model and extended this model for simulating sharp crack tip SENB. Figure 4.10 shows the meshing used for the simulation of crack tip sharpness effect on fracture toughness vs. crack growth.

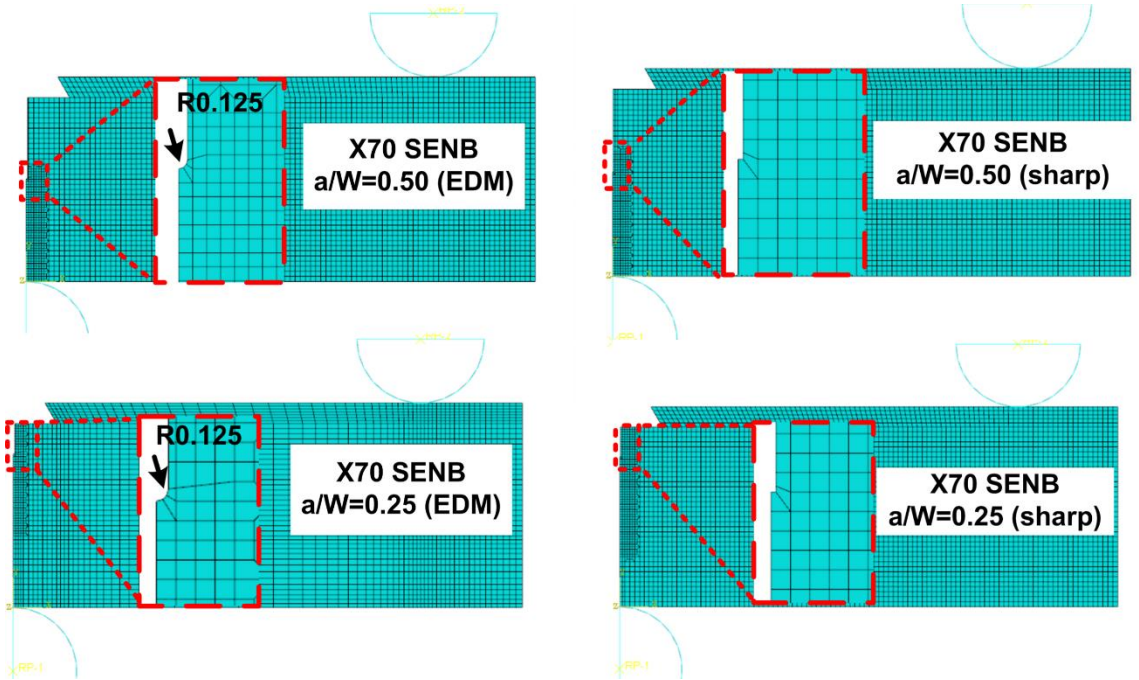


Figure 4.10: Meshing followed by SENB with EDM cut crack and sharp crack.